Titanium Nitride (TiN) Germination and Growth during Vacuum Arc Remelting of a Maraging Steel

Vincent Descotes [1,2], **Thibault Quatravaux** [1,*], **Jean-Pierre Bellot** [1] and **Sylvain Witzke** [2] and **Alain Jardy** [1]

[1] Institut Jean Lamour (UMR 7198 Université de Lorraine/CNRS), Campus Artem, 2 allée André Guinier-BP 50840, LabEx DAMAS, CEDEX, F-54011 Nancy, France; vincent.descotes@aperam.com (V.D.); jean-pierre.bellot@univ-lorraine.fr (J.-P.B.); alain.jardy@univ-lorraine.fr (A.J.)

[2] APERAM Alloys Imphy, BP1 Centre de recherches P. Chevenard, F-58160 Imphy, France; sylvain.witzke@aperam.com

[*] Correspondence: thibault.quatravaux@univ-lorraine.fr;

Abstract: During the processing of maraging steels, Titanium easily combines with Nitrogen to form nitride inclusions, known to be deleterious for fatigue properties of the alloy. According to thermodynamic calculations, the precipitation occurs during solidification of the vacuum arc remelted (VAR) ingot. A coupled model of titanium nitride (TiN) inclusion precipitation and vacuum remelting has been set-up to study the inclusion cleanliness of the ingot. The nitrogen content, nuclei numeral density and solidification time appear as the key factors which control the inclusion size.

Keywords: nucleation; TiN inclusions; maraging steel; VAR process

1. Introduction

Non-metallic inclusion (NMI) cleanliness is a major factor influencing the mechanical properties of metallic alloys, such as the fatigue strength. The steelmaking company Aperam Alloys, located in Imphy (France), produces various grades of maraging steel. We will focus our attention on one given grade, namely 18% Ni, 9% Co, 5% Mo and 0.45% Ti, with residual Nitrogen, for which titanium nitride (TiN) inclusions represent the most harmful NMI. They are easily detected with an optical microscope, as they form yellow angular particles, as shown in Figure 1. Several authors, including Morita and Kunisada [1], and more recently Kim et al. [2], have studied the thermodynamic conditions for their nucleation and growth, concluding that these stable inclusions nucleate during the alloy solidification (see Section 2.1).

Vacuum arc remelting (VAR—see Figure 2) is generally used to process high value metallic alloys. The alloy to be remelted is first prepared in a VIM furnace. The VIM ingot constitutes the electrode in the VAR melt. A DC electric arc, generated between the electrode (cathode) and the base of a Cu mould in a vacuum atmosphere, provides a high amount of heat that melts the electrode. The arc is maintained all along the remelting operation between the electrode and the growing secondary ingot. Such remelting provides a better control of the solidification of the final ingot and benefits from the vacuum to enhance refining of the material [3].

The objective of the present work is to assess the origin and size of TiN particles in the remelted ingot. A predictive model is first developed to simulate germination and growth of TiN phase during solidification of the alloy, as well as the size distribution of the corresponding inclusion population and the associated depletion in Ti and N in the liquid phase. This modelling approach is then coupled with the CFD 2D axisymmetric model SOLAR, previously developed in Nancy [4] to simulate the VAR

process. Such an association enables one to estimate the inclusion cleanliness in the remelted ingot. Simulation results are finally compared to a full-scale ingot specifically remelted by Aperam Alloys. The coupled model stresses the heterogeneous size distribution of inclusions in VAR ingots and can be further used for process optimization.
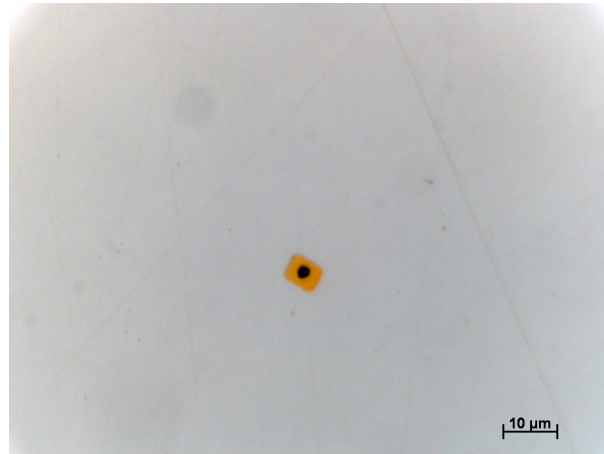
Figure 1. Micrograph of a titanium nitride (TiN) particle at the surface of an etched maraging steel sample.
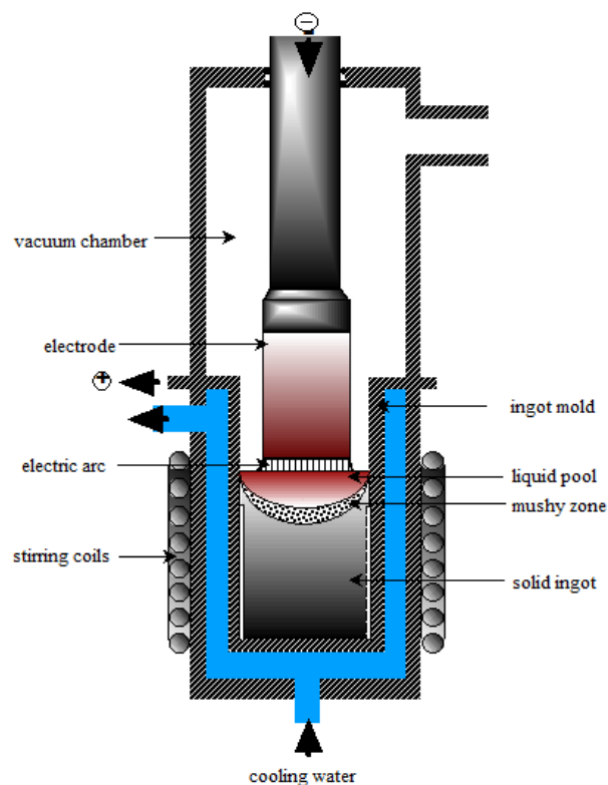
Figure 2. Sketch of the VAR process.

2. Background

2.1. Thermodynamical Properties of TiN Inclusions

TiN precipitation is governed by the interfacial chemical reaction Ti + N $\rightleftarrows$ TiN(s), characterized by its solubility product $K_{TiN}(T)$ which is related to the activities of solutes in the liquid steel at equilibrium through:

$$K_{TiN}(T) = a_{Ti}^{eq} \cdot a_{N}^{eq} \tag{1}$$

Table 1 reports some numerical values for the solubility product of TiN in pure liquid iron, as found in the literature.

Table 1. Solubility product of TiN in pure liquid iron as a function of temperature.

Ref.	$\log_{10} K^{\%}_{TiN}$
[5]	$\dfrac{-16433}{T} + 6.19$
[1]	$\dfrac{-19800}{T} + 7.78$
[2]	$\dfrac{-15780}{T} + 5.63$

The interaction between the solutes and liquid steel are captured by an activity coefficient γ_X, so that activities can be directly computed from the mass fractions with the formula:

$$a_X = \gamma_X \cdot \omega_X \tag{2}$$

Using the software Thermo-Calc [6] with TCFE7 Steels/Fe-alloys database version 7 [7] to compute the composition at equilibrium, the value of the solubility product of TiN in a maraging steel near the liquidus temperature is found to be:

$$\frac{K_{TiN}}{\gamma_{Ti} \cdot \gamma_N} = 7.8 \cdot 10^{-8} \tag{3}$$

Assuming 4500 ppm of Titanium in the liquid bath, the associated saturation content of Nitrogen corresponds to 17 ppm. Since a low Nitrogen content of 10 ppm is commonly reached after Vacuum Induction Melting, any TiN inclusion that may be transferred from the VAR electrode to the ingot liquid pool is unstable and will dissolve before alloy solidification. However, at that moment, solidification-induced segregation will make the local solute concentrations in the interdendritic liquid rise above the solubility limit, therefore triggering the precipitation of nitrides.

2.2. VAR Process Simulation

Modelling the VAR process has been successfully attempted over the past decades. Result of these efforts are collected into many calculation codes, like BAR [8], MeltFlow [9] or SOLAR [4,10,11], for example.

The SOLAR software (which stands for SOLidification during Arc Remelting) has been developed in Nancy through several PhD works [4,12,13] since 1995. The model is a 2D-axisymetric transient-state finite volume code describing ingot growth, solidification and cooling. It solves the coupled electromagnetic, solute, momentum and heat transport equations. Water cooling of the copper mold, as well as the injection of He gas in the gap between the ingot side and mold, are modeled with thermal resistances.

The numerical treatment of convective phenomena is based on a first order upwind numerical scheme [14]. The mesh is refined at the ingot top and side. The growth of the ingot is performed by periodically adding new cells in the upper part of the ingot, which results in introducing advective source terms in the numerical scheme [15].

The model takes into account all volume forces applied upon the liquid phase during remelting, to provide a fine description of the pool hydrodynamics. The partially solidified (i.e., "mushy") zone is described as an isotropic porous medium, whose permeability is calculated with a classical Kozeny–Carman relation and implemented in the momentum transfer equation.

The recirculation flow in the melt pool results from a competition between the following main phenomena in the in-plane (r,z) that are all taken into account in SOLAR:

- Natural convection, mainly due to thermal gradients, that generates a downward flow near the crucible wall and an upward flow in the center region;
- The Lorenz force created by the interaction between the melting current and self-induced magnetic field, localized near the ingot top;
- Possibly, the centrifugal force induced by the e.m. stirring caused by an external magnetic device.

The mathematical model has been extensively validated through comparison between calculated and experimental liquid pool profiles for Ti and Zr alloy remelted ingots [10,16], as well as steel and Nickel-based superalloys [11,17].

2.3. Modelling of Inclusion Formation

In the literature, the formation of various NMI has been modeled. As an example, Lei et al. [18] focused on Ostwald ripening of alumina inclusions, while Matsumiya [19] considered phase change inside MnS inclusions and engulfment, but did not introduce a size analysis of these inclusions. Also, observations of TiN inclusions are widely reported. In particular, Ohta and Suito [20] experimentally characterized the effect of the germs on TiN particle size, showing the benefit of MgO particles to increase the numeral density of inclusions and thus reduce their size.

On the contrary, only few authors have proposed a specific mathematical modeling of TiN precipitation. Rocabois et al. [21], then Lehmann et al. [22], who considered heterogeneous nucleation and diffusion kinetic laws with no engulfment, carried out a study of TiN particles germination and growth during solidification.

3. 0D Precipitation Model

In this work, the precipitation of a TiN inclusion is considered to take place during solidification thanks to solute enrichment in the liquid phase (i.e., microsegregation). A model is developed for a 0D case (solidification of a closed system) as briefly described in a previous study [23], with a more accurate numerical treatment of the constitutive equations.

Any TiN inclusion is assumed to form upon an inert preexisting oxide that acts as a nucleus. This hypothesis is consistent with optical microscope observations which reveal such compounds for a large majority of TiN inclusions. A TEM observation reported by Descotes et al. [24] shows an orientation relationship between a TiN particle and its germ. Nucleation is therefore considered to be only heterogeneous.

The calculation domain is a closed system, that does not exchange solute nor particles with the outside. It is also considered that the precipitation reaction stops in the solid phase. This assumption is supported by the fast cooling rate of the VAR ingot, which prevents the establishment of a significant solid-state diffusion to pursue precipitation.

3.1. Inclusion Precipitation

A sketch of the system is provided in Figure 3. Competition takes place between the solidification-driven partition which continuously redistributes Titanium and Nitrogen in the liquid phase (see Section 3.3) and the precipitation which consumes the solutes.

All equations are written in terms of the molar concentrations of element X. This choice simplifies the derivation of molar balance equations. It is then possible to deduce the mass fraction from the molar concentration by using the following relationship:

$$\omega_X = C_X \frac{M_X}{\rho_{steel}} \tag{4}$$

where ω_X is the mass fraction of element X, C_X its molar concentration (mol·m^{-3}), M_X its molar mass (kg·mol^{-1}), and ρ_{steel} the density of the alloy (kg·m^{-3}).

The supersaturation is defined as the ratio of activities of the corresponding precipitating elements to the solubility product [21]:

$$S = \frac{\gamma_N \cdot \gamma_{Ti} \cdot C_{Ti} \cdot C_N}{K_{TiN}} \qquad (5)$$

The nucleation model is derived from a similar one developed for computing athermal nucleation of solid particles [25]. It is based on the computation of the Gibbs energy variation of an elemental volume of supersaturated liquid:

$$\Delta_{mol}G = -R\,T \cdot \ln S \qquad (6)$$

where $\Delta_{mol}G$ is the molar Gibbs energy of the nucleation (J·mol^{-1}), R the ideal gas constant (J·mol^{-1}·K^{-1}), T the temperature (K) of the liquid steel.

Considering a spherical inclusion with a radius r, the overall free energy variation $\Delta_{total}G$ includes the volume Gibbs energy change due to the precipitation and the induced energy modification from the creation of the interface between TiN and steel :

$$\Delta_{total}G(r) = \frac{4}{3}\,\pi\,r^3\,\frac{\rho_{TiN} \cdot \Delta_{mol}G}{M_{TiN}} + 4\,\pi\,r^2 \cdot \Gamma_{TiN/steel} \qquad (7)$$

where $\Gamma_{TiN/steel}$ is the interfacial energy of TiN in the steel (J·m^{-2}), M_{TiN} the molar mass of TiN (mol·kg^{-1}), and ρ_{TiN} the TiN density (kg·m^{-3}).
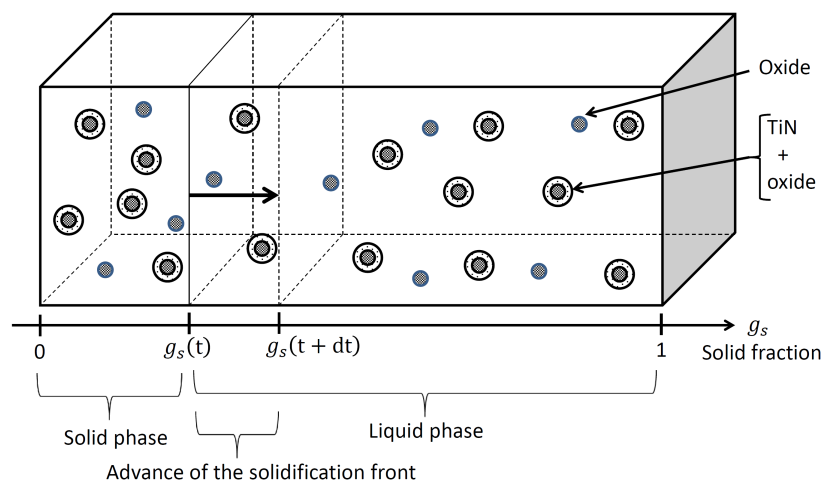

Figure 3. 0D system modeled.

According to Equations (6) and (7), the chemical enthalpy term is a driving force for nucleation when S $\geq$ 1, whereas surface tension acts against precipitation. As a consequence, in order to create nuclei, the supersaturation in the liquid should be high enough to compensate the creation of a new surface. Therefore, r_{nucl}^{TiN}, the critical radius for a stable nuclei, is deduced from the minimization of Equation (7). Finally, the curvature radius of a stable TiN nucleus depends on the supersaturation [26]:

$$r_{nucl}^{TiN} = \frac{2\,\Gamma_{TiN/steel}\,M_{TiN}}{R\,T\,\ln S\,\rho_{TiN}} \qquad (8)$$

It is considered that nucleation always takes place upon a spherical oxide of radius Φ. The curvature radius of the TiN nucleus should be high enough to enable the connection on the underlying oxide in accordance with the wetting angle of the TiN on the oxide θ:

$$r_{nucl}^{TiN}\,\sin\theta \leq \Phi \qquad (9)$$

This geometric condition combined with equation 6 induces the existence of a minimum supersaturation S_g, needed to activate a given oxide as a nucleation site for a TiN inclusion:

$$S_g = \exp\left(\frac{2\,\Gamma_{TiN/steel} \cdot \frac{M_{TiN}}{\rho_{TiN}} \cdot \sin\theta}{RT\phi}\right) \tag{10}$$

3.2. Growth of the TiN Inclusions

In order to compute the particle size evolution, the model considers the following kinetic law:

$$G = \frac{dr}{dt} = k_c\,(S-1) \tag{11}$$

where r is the instantaneous radius of an oxide-TiN assembly (m), G is the growing rate of the inclusion, S the supersaturation, and k_c a kinetic factor which represents the interfacial chemical reaction rate as well as Ti and N mass transport from the supersaturated bulk liquid to the TiN particle surface.

Inspired by a similar model from Lehmann et al. [22], this relation describes the fact that the more the bath is supersaturated, the faster an inclusion will grow. Ti and N solutes play an equal role in the mechanism of inclusion growth.

From the growing rate, a transport equation in the internal coordinate space (inclusion size) for the particle distribution can be derived:

$$\frac{\partial n^l_{TiN}(r,t)}{\partial t} = -G\,\frac{\partial n^l_{TiN}(r,t)}{\partial r} \tag{12}$$

where $n^l_{TiN}(r,t)$ is the size distribution of TiN in the liquid phase (density number of inclusions of radius r per unit volume of liquid metal and per unit length of particle radius).

This differential equation is similar to a classical advection equation encountered in fluid flow modeling. Its resolution is performed using a semi-analytical scheme, as detailed in the Appendix A.

The inclusion size distribution is related to the overall particle concentration through the equation:

$$C^l_{TiN}(t) = \frac{\rho_{TiN}}{M_{TiN}}\left[\int_0^{+\infty} n^l_{TiN}(r,t)\frac{4}{3}\pi r^3 dr - \int_0^{+\infty} n^l_{OxAct}(\Phi,t)\frac{4}{3}\pi r^3 d\Phi\right] \tag{13}$$

where $n^l_{OxAct}(\Phi,t)$ is the size distribution of oxides which have been activated (density number of oxides of radius Φ per unit volume of liquid metal and per unit length of oxide radius).

3.3. Solidification and Segregation

The solutes (Ti and N) are distributed between the solid phase, the liquid phase, and the TiN inclusions located in both phases:

$$C^{tot}_X = g_s\,(C^s_X + C^s_{TiN}) + (1-g_s)(C^l_X + C^l_{TiN}) \tag{14}$$

where g_s is the solid fraction of the system, supposed to depend on the temperature through a predefined solidification path, specific to the alloy.

In the rest of this section (0D model), a simple linear evolution of the temperature with time is set. This is a very strong approximation; however, the aim of this model is to study the link between segregation and precipitation.

A lever rule is used to describe the solidification of the alloy, thus assuming infinite diffusion of the solutes within both solid and liquid phases, as discussed in the reference book by Kurz and Fischer [27]. The concentrations of element X dissolved in the solid and liquid phase are linked by:

$$C^s_X = k_X \cdot C^l_X \tag{15}$$

where k_X is the partition coefficient of element X.

From the assumption of a closed system, C_X^{tot} is constant. Therefore, differentiating Equation (14) leads to:

$$dC_X^{tot} = (C_X^s - C_X^l)\, dg_s + g_s\, dC_X^s + (1 - g_s)\, dC_X^l + d\,(g_s \cdot C_{TiN}^s) + d((1 - g_s)\, C_{TiN}^l) = 0 \quad (16)$$

and, after combining Equations (13) and (14):

$$dC_X^l = \underbrace{\frac{(1 - k_X)\, C_X^l\, dg_s}{1 - (1 - k_X)g_s}}_{\text{segregation}} - \underbrace{\frac{d((1 - g_s)\, C_{TiN}^l)}{1 - (1 - k_X)g_s}}_{\text{precip.in liq. \& engulf.}} - \underbrace{\frac{d(g_{(s)}\, C_{TiN}^s)}{1 - (1 - k_X)\, g_s}}_{\text{precip.in sol.\& engulf.}} \quad (17)$$

A time-splitting scheme is used to solve numerically this equation: The segregation part is solved in a first stage. Then the engulfment of particles is calculated (Section 3.4) for a given solid fraction. Finally the consumption of solutes by precipitation of inclusions in the liquid is computed. As stated previously, no precipitation in the solid phase is taken into account.

3.4. Engulfment of the Inclusions

As solidification proceeds, the solidification front engulfs some TiN inclusions from the liquid into the solid. Those inclusions will no more be available in the liquid to grow further, so they become inert (as stated previously, the model assumes no diffusion of solutes in the solid phase–hence no growth–at the macroscopic scale).

Considering a uniform spatial distribution of the TiN inclusions in the liquid phase at each moment, the solidification of a fraction dg_s during time interval dt transfers the density $\alpha(r)\, n_{TiN}^l(r, t)dg_s$ of TiN inclusions of radius r from the liquid to the solid phase. The following set of equations is therefore obtained:

$$d(g_s\, n_{TiN}^s(r, t)) = \alpha(r)\, n_{TiN}^l(r, t)\, dg_s$$
$$d((1 - g_s)\, n_{TiN}^l(r, t)) = -\alpha(r)\, n_{TiN}^l(r, t)\, dg_s \quad (18)$$

The engulfment coefficient $\alpha(r)$ accounts for a possible partial rejection of TiN at the solidification front. Since the size of TiN (several micrometers) is two orders of magnitude smaller than the primary dendrite arm spacing of the remelted Maraging steel (several hundred of micrometers), we assume that rejection is negligible, so no restriction is set on the engulfment of an inclusion into the solid phase. In the rest of this article, it will be considered that, whatever the inclusion radius, $\alpha(r) = 1$. In such condition, the set of Equations (18) reduces into:

$$d(g_s\, n_{TiN}^s(r, t)) = n_{TiN}^l(r, t)\, dg_s$$
$$d\, n_{TiN}^l(r, t) = 0 \quad (19)$$

4. Numerical Results—0D Model

4.1. Nominal Case

First, a nominal case has been simulated with the 0D model. The nitrogen content in the alloy is 10 ppm. The total oxide number density is 10^{11} oxides per cubic meter. The oxide size distribution (between 0.4 μm and 1 μm in radius, as shown in Figure 4) is based on experimental observations.

For this nominal case, the solidification time (time during which the temperature varies linearly (Section 3.3) from liquidus to solidus) is 1000 s. Figure 5 presents the computed size distributions after full solidification: activated oxides which have served as nuclei for nitrides, nitrides in the solid phase, and nitrides in the ultimate drop of liquid phase. The latter is recalled here just to facilitate

the comprehension of the model. The only observable distribution after complete solidification would be the one in the solid phase.
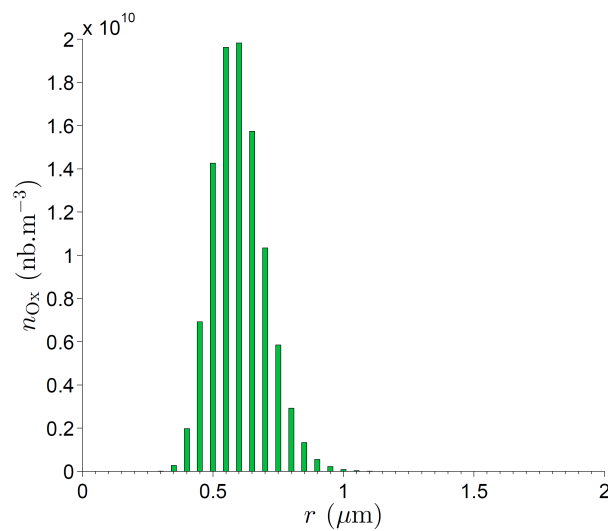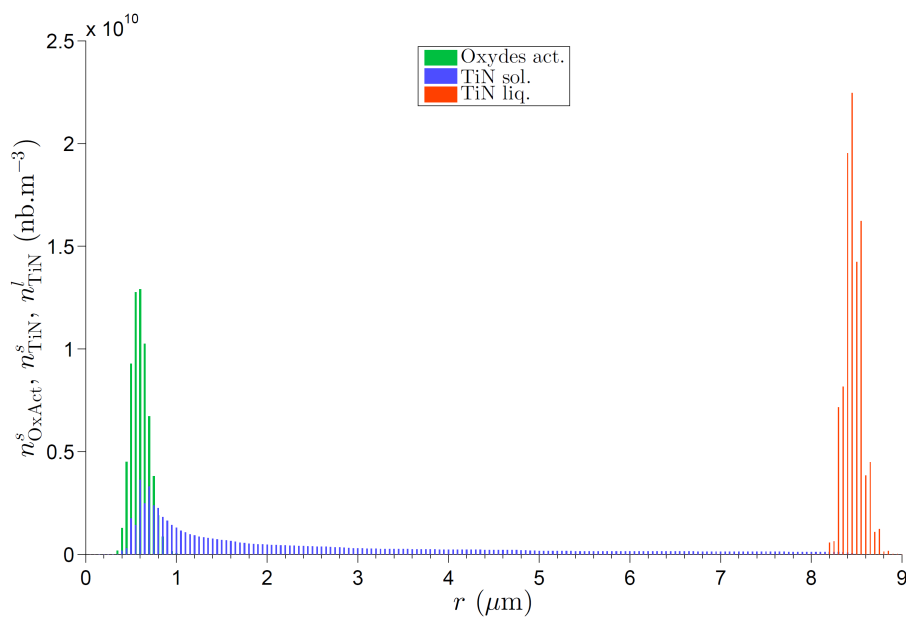
Figure 4. 0D model—Oxide size distribution.

Figure 5. Final computed TiN size distributions in the (residual) liquid and solid phase, and activated oxides size distribution.

Whatever the oxide radius, the nucleation minimum supersaturation S_g (see Equation (10)) is close to 1. Thus, every oxide that is not engulfed first in the solid phase actually acts as a nucleus for nitrides. Because of the continuous growth of the particles, the TiN distribution in the liquid is transported through the upper radii almost without altering its shape. The small shape discrepancy is caused by numerical artefacts. On the contrary, the distribution of TiN inclusions in the solid phase exhibits a very different shape, because of the engulfment phenomenon: once engulfed in the solid, TiN particles become inert, whereas those in the liquid pursue their growth. The final distribution is spread out on every radius between the smallest oxide (0.4 µm) and the largest TiN in the ultimate liquid phase (8.8 µm). It can be seen that the highest densities are achieved for inclusion radii smaller than 2 µm, nevertheless densities corresponding to a large final radius are not negligible (see the enlargement on Figure 6).
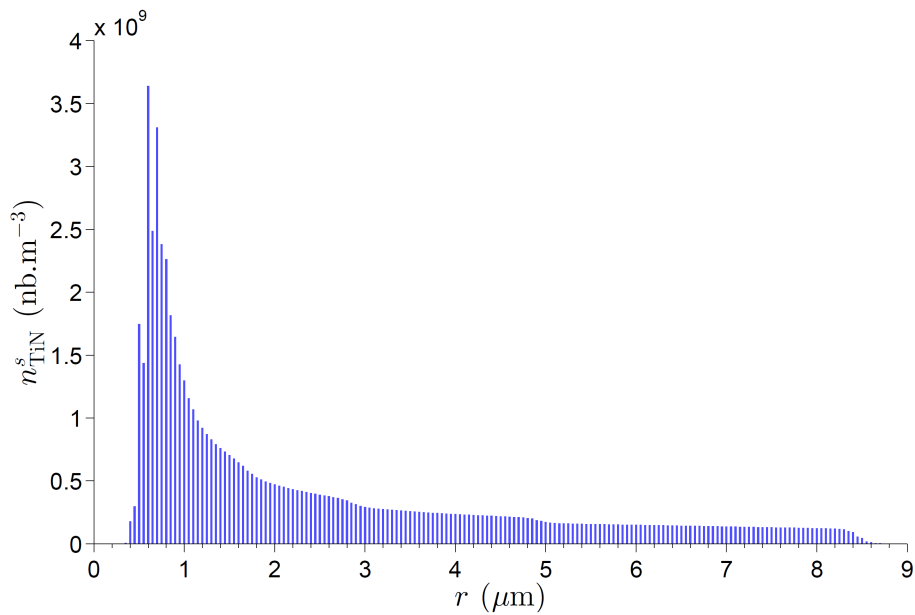
Figure 6. Final computed TiN size distribution in the solidified material.

An important result is the size of these largest particles. In the rest of the paper, we will use systematically the model output r_{97} , which is defined such as 97% of the TiN inclusions in the solid have a radius smaller than r_{97} . In the nominal case, the predicted r_{97} value is 7.5 µm.

4.2. Influence of Some Parameters

First of all, the total oxide number density obviously impacts the total number density of TiN inclusions that will nucleate. By increasing this parameter, a higher quantity of solutes is consumed by the inclusion precipitation, so that the growing rate of each one is expected to decrease. Therefore, smaller inclusions should result. Figure 7 presents the radius r_{97} of the final TiN distribution as a function of the nuclei density.
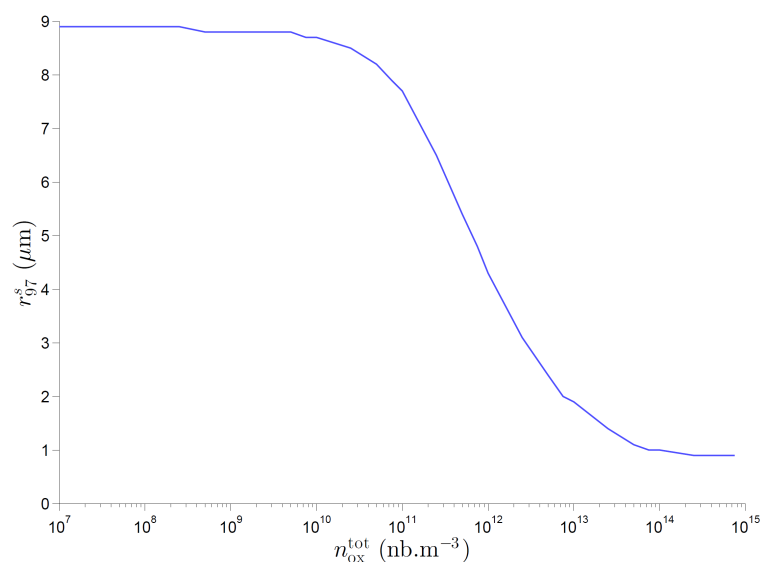

Figure 7. Influence of the oxide density on the size of largest inclusions in the solid phase. (ω_N = 10 ppm, t_s = 1000 s).

In a semi-logarithmic scale, the figure curve shows an inverted S-shaped curve with two horizontal asymptotes:

- For low oxide densities (below 10^{10} oxides·m^{-3}), the radius r_{97} tends toward a constant value 8.9 µm. This asymptote results from the negligible consumption of solutes by the inclusions, as compared to the quantities released by solute redistribution (i.e., segregation). This segregation evolves as if no precipitation occurred, leading to an identical growing rate, whatever the TiN number density in the bath.
- From 10^{10} to 10^{14} oxides per cubic meter, precipitation influences significantly the solute content. The inclusion size decreases with the increase in nuclei density.
- Above 10^{14} oxides·m^{-3}, the precipitation consumes so much solute content that the supersaturation (see equation 9) remains close to one, leading to a very low growing rate. The asymptote corresponds to the upper radius of the nuclei (0.8 µm).

Secondly, the duration left for the precipitation reaction to take place (i.e., the solidification time) conditions the influence of TiN precipitation on the segregation and particle growing rate. Figure 8 illustrates this effect with a solidification time varying from 200 to 1400 s.
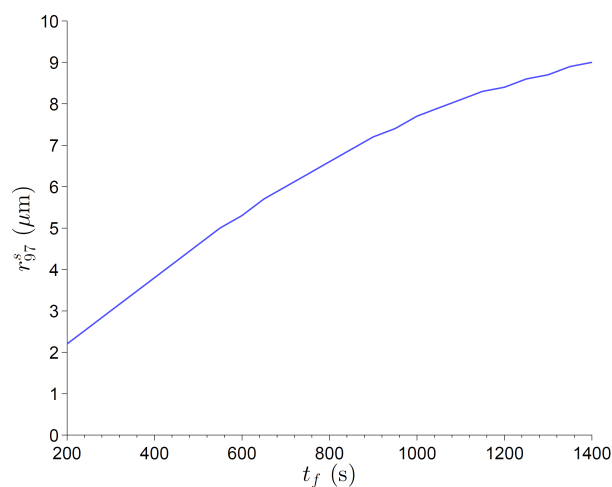

Figure 8. Influence of the solidification time on the size of largest inclusions in the solid phase. (ω_N = 10 ppm, oxide density = 10^{11} m^{-3}).

In the cases studied, the final inclusion size globally increases with the solidification time. This is the result of a kinetic effect (more time is allowed to make the particles grow), moderated because of the and the coupling with segregation (the solute consumption is higher, thus reducing segregation). In other cases, a maximum was sometimes observed (see [23]), whose position depended on the model parameters (kinetic constant, oxide number density, solubility product and partition coefficients).

Thirdly, the overall Nitrogen content plays a key role in the model as N is by far the limiting reactant. Figure 9 shows the evolution of r_{97} with the Nitrogen mass fraction. Obviously, this radius increases with ω_N.

This curve shape derives from the following: first, increasing the Nitrogen mass fraction increases the supersaturation, hence the growing rate of the particles. However, such growth induces an increase in the solute consumption, leading to a decrease in segregation and supersaturation, thus of the growing rate.

Below 1.6 ppm of Nitrogen, precipitation does not occur. It should be stated, however, that infinite diffusion of Ti in the solid phase is possibly a wrong assumption. By replacing it with a Gulliver–Scheil model or a retro-diffusion assumption (Kurz–Fischer model [27]), higher segregation can be reached in the interdendritic liquid (for example, see [16]), which may trigger the precipitation for a lower Nitrogen content.
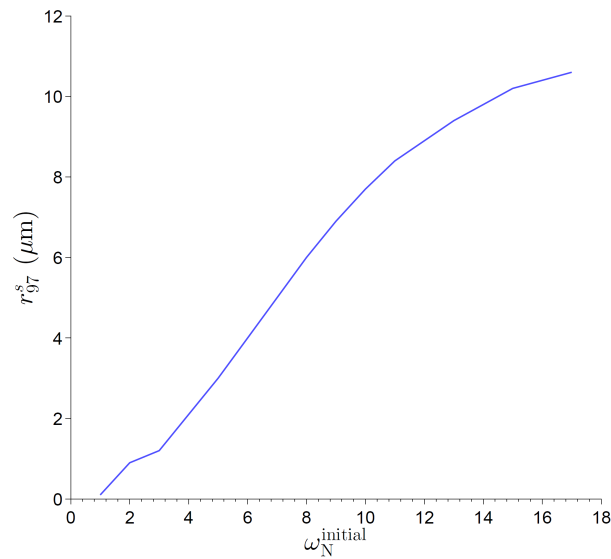
Figure 9. Influence of the overall Nitrogen content on the size of largest inclusions in the solid phase. (t_s = 1000 s, oxide density = 10^{11} m^{-3}).

5. Coupling with SOLAR Model

In this section, the CFD macromodel SOLAR described in Section 2.2 is coupled with the 0D precipitation model. The latter is applied in each mesh cell in the mushy zone: the variation in g_s and the segregation computed by SOLAR determine the inclusion behavior: germination (Equation (10)), particle growth (Equation (10)), solute consumption (Equation (17)), and engulfment (Equation (19)). The interaction between the cells is achieved through the solute transport equation solved in SOLAR. The particles are supposed to be immobile in the interdendritic liquid before engulfment.

In order to validate the full model, Aperam Alloys has remelted a specifically designed ingot in its Imphy plant.

5.1. Validation Remelting

It is noteworthy that usual industrial parameters differ from the specific conditions chosen to process the validation ingot. As the electrode melt rate is known to have a major influence on the ingot solidification, it is also expected to be a key parameter on inclusion cleanliness. Two melt rates were defined to cast the validation ingot, with abrupt modifications of the process conditions between the two permanent regimes. At the end of the remelting, a sudden cut of the electrical input was applied in order to freeze the remaining liquid pool.

5.2. Analysis Procedure

A longitudinal slab was extracted from the remelted ingot and divided into several parts. Then, each piece was polished and etched using FRY7 reactant (HCl + CuCl$_2$) to reveal the solidification structure. Moreover, some liquid pool shapes were reconstructed on the assumption that the direction of the columnar dendrites remains perpendicular to the solidification front.

Three samples were extracted at different heights along the axis for inclusion analysis. An automated counting of all inclusions on each polished sample was performed using the optical microscope. The surface of each inclusion was measured, then converted into an equivalent radius through:

$$r_i = \sqrt{\frac{S_{incl}}{\pi}}$$

(20)

This counting provides a sequence of n inclusion radii that can be sorted in ascending order r_i. The size distribution of the inclusions was approximated by a log-normal law with two parameters μ and θ. The cumulative distribution function of this law is expressed by:

$$F(r; \mu, \theta) = \frac{1}{2} + \frac{1}{2} \, erf \left(\frac{\ln r - \mu}{\theta \sqrt{2}} \right)$$

(21)

The smallest particles are not correctly detected by the optical microscope: a threshold is set at a radius of 2.5 µm. This prevents one to measure directly the total number density of particles which are present on the sample. Therefore, this data has to be estimated: a fit is performed with a non-linear least square method on the cumulative number of particles i sorted in ascending order:

$$i = n_{tot} \, (F(r_i; \mu, \theta) - F(r_1; \mu, \theta))$$

(22)

where n_{tot} is the total number of particles that are present on the sample, i the particle index in the sequence r_i of increasing radii, and r_1 the smallest radius of the sequence. It leads to an estimation of n_{tot}, μ and θ. The total volume density of particles can be derived from the surface one $n^s_{tot} = \frac{n_{tot}}{S}$ assuming a uniform spatial distribution of the particles on the sample:

$$n^v_{tot} = \frac{3\sqrt{\pi}}{4} (n^s_{tot})^{\frac{3}{2}}$$

(23)

Parameters μ and σ are related to the mean radius and root mean square radius by:

$$\begin{cases} r_{average} = \exp \left(\mu + \frac{\sigma^2}{2} \right) \\ r_{sig} = (e^{\sigma^2} - 1) \cdot e^{(2\mu + \sigma^2)} \end{cases}$$

(24)

Finally, an estimation of the experimental value of r_{97} is deduced from the definition of the cumulative function of the log-normal law (equation 21):

$$r_{97} = \exp \left(\sigma \sqrt{2} \, erf^{-1}(2 \times 0.97 - 1) + \mu \right)$$

(25)

where erf^{-1} is the inverse error function.

5.3. Experimental Observation

Results from the inclusion counting methodology on the three samples, based on a log-normal law, are reported in Table 2, while Figure 10 presents the metallurgical structure of the longitudinal slab. Liquid pool profiles have been drawned, based on the microstructure, assuming that the solidification front is always perpendicular to columnar dendrites.

Table 2. Size of the largest inclusions (r_{97}) in the samples taken from the ingot near the axis.

Height (m)	r_{97} (µm)	Comments
0.54	4.2	Low melt rate
0.85	3.0	Low melt rate
1.28	3.7	High melt rate

(a)

(b)

Figure 10. Metallurgical structure revealed on an axial section of the ingot. ((**a**): top part—(**b**): bottom part).

Comparing liquid pool profiles in the top part (Figure 10a, dotted line) to the bottom zone (Figure 10b, full line), we can notice that a higher melt rate increases the liquid pool depth. The deep pool shape at the end of the remelting is easily observed thanks to the equiaxed solidification in the last pool. Such structure was generated by the sudden stop in the melting current, without any hot-topping procedure.

5.4. Numerical Results—Fully Coupled Model

All operational data (melting current, arc voltage and melt rate) for the validation melt were stored during the actual remelting, and used as input for the simulation.

5.4.1. Temperature Maps

Computed temperature maps of the remelted ingot at several moments during the remelting are presented in Figure 11. The mushy zone can be identified between the black full lines corresponding to liquidus and solidus isotherms. SOLAR predicts an extension of the mushy zone in the end of the remelting, when the high melt rate regime is reached. Comparison of Figures 10 and 11 confirms the validation previously obtained on a wide range of metal alloys, such as special steel [15], titatium alloys [10] and nickel-based superalloys (Inconel 718) [11].
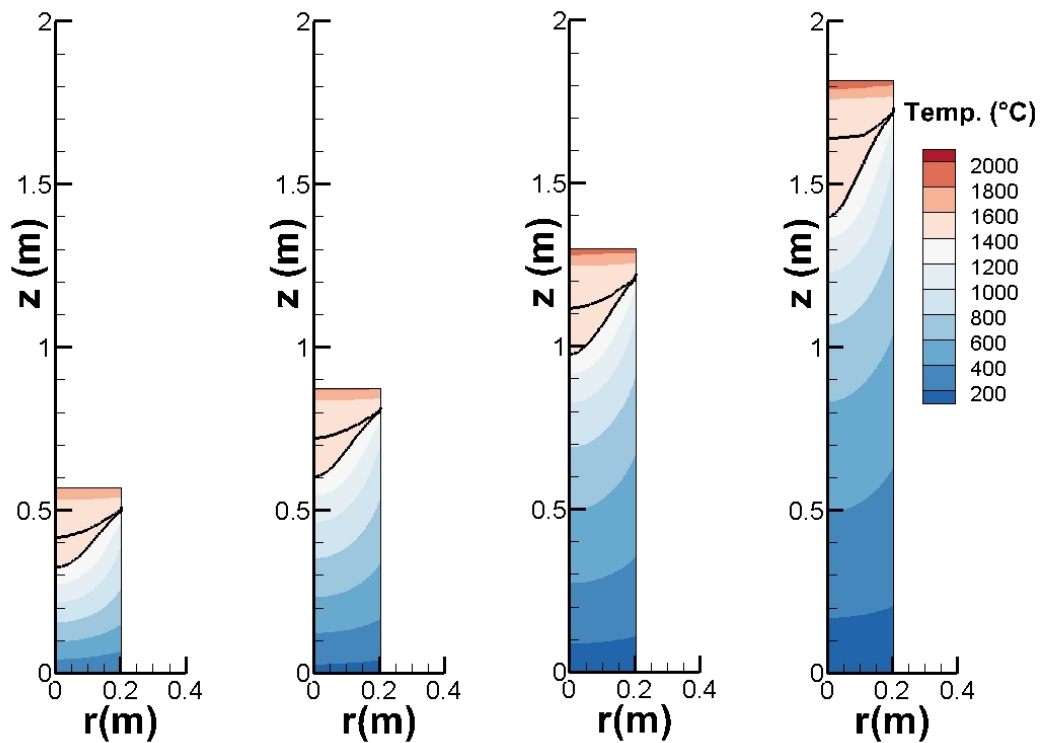
Figure 11. Computed ingot temperature map at different moments during the remelting.

5.4.2. Repartition of the Inclusion Population

Inclusion cleanliness is numerically assessed through the radius r_{97} (the upper bound radius of 97 % of TiN distribution) and final TiN mass fraction (Figure 12). It is noteworthy that macrosegregation of Ti and N play an important role in TiN precipitation, as shown on maps. In this simulation, solidification of the last pool was not considered.
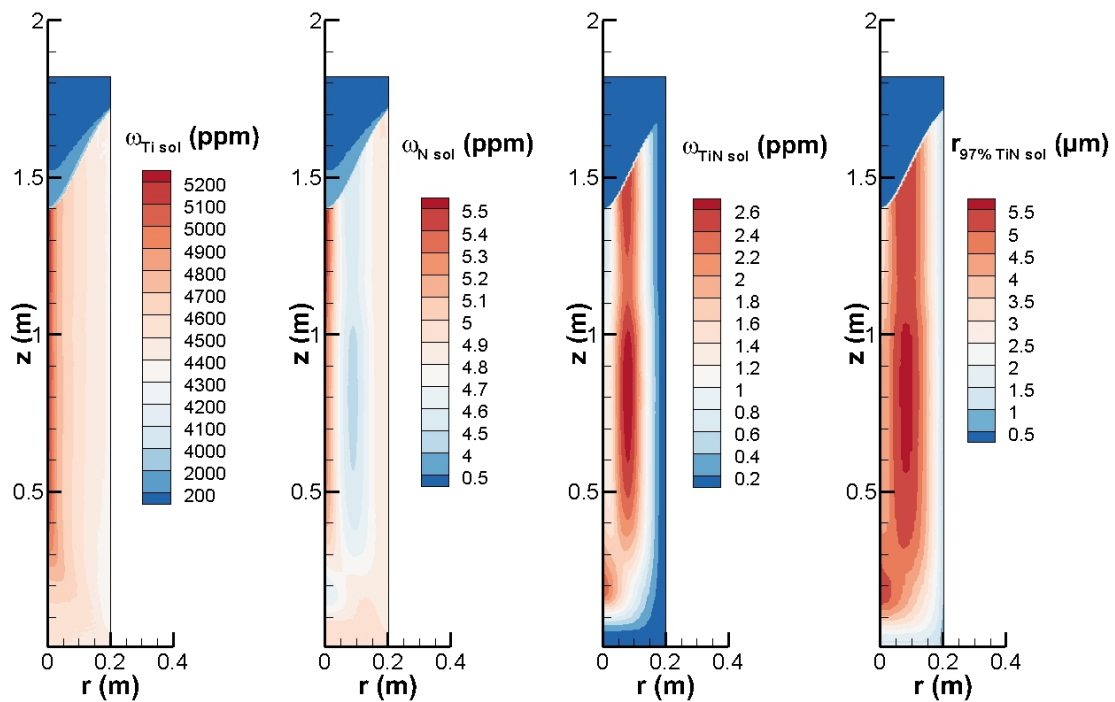

Figure 12. Computed cleanliness of the remelted ingot.

Figure 12 shows that the maximum computed size of r_{97} (the largest TiN inclusions) is located in the bottom part of the ingot, which has been remelted with a low melt rate, and all along the mid radius. The model predicts smaller inclusions in the high melt rate zone (ingot upper half). A pronounced positive macrosegregation of N and Ti is visible near the symmetry axis. It is generated by the association of the partition during alloy solidification and the buoyancy-driven recirculation of the liquid metal pool, with an ascending flow in this zone. The maximal value of r_{97} calculated for this simulation is about 5.5 µm.

On Figure 13, a profile was extracted along the central axis and compared to experimental data from Table 2 (see Figure 13). The magnitude order seems well predicted, although the exact experimental shape is not captured.
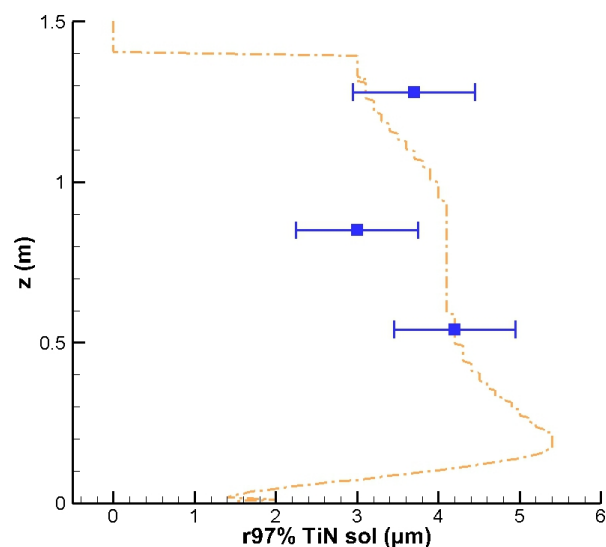

Figure 13. Comparison between the computed centerline r_{97} (dotted line) with the observation.

6. Conclusions

Thermodynamic calculations show that TiN inclusions are unstable in the liquid maraging steel bath. Segregation in the mushy zone during solidification rises Ti and N content in the interdendritic liquid, making the precipitation reaction possible. A 0D precipitation model was set up to study the coupling between these two phenomena. The parametric study highlights three key parameters for the size of the largest inclusions: the Nitrogen mass fraction, the nuclei number density, and the solidification time.

The thermodynamic model was then coupled with the CFD macromodel SOLAR in order to describe the behavior of the TiN inclusion population during vacuum arc remelting of a maraging steel. The simulation was run, using as input the actual process conditions of a validation melt specifically designed for this purpose, including two successive regimes (low then high melt rate). Calculations show that:

- Inclusion size is heterogeneous all along the radius, and largest inclusions are localized in a mid-radius zone.
- The melt rate influences the inclusion size, as it modifies the local solidification time.

Obviously, new validation melts with different operating conditions are required in a further study. Also, it should be noticed that using a Gulliver–Scheil model or a back-diffusion model would probably improve the description of Titanium segregation.

Author Contributions: Conceptualization, A.J., J.-P.B. and S.W.; investigation, V.D.; visualization, V.D.; supervision, A.J., J.-P.B. and S.W.; writing—original draft preparation, V.D.; writing—review and editing, A.J., J.-P.B. and T.Q. All authors have read and agreed to the published version of the manuscript.

Conflicts of Interest: The authors declare no conflict of interest

Appendix A. Numerical Resolution of the Growth Equation

The growth Equation (12) is identified as a pure convective transport equation. An analytical solution can be found using the method of characteristics to express the evolution of the radius of an inclusion with time:

$$r(t) = r(t_0) + G \cdot (t - t_0) \tag{A1}$$

If several inclusions share the same initial radius, they form a peak distribution which continuously shifts its radius without changing its number density value:

$$n^l_{TiN}(r, t + \Delta t) = n^l_{TiN}(r - G \cdot \Delta t, t) \tag{A2}$$

Any distribution of TiN particles can be discretized in severalclasses with different number densities of inclusions in each radius class. Couples of radii and number densities $(r; n^l_{TiN})$ are then created.

Equation (A1) indicates that the number density of each peak should be conserved. When growing, the true radius of a peak will fall between two bounds of the radial discretization, called pivots. A peak will therefore be distributed on its two adjacent classes, so that the average of the two classes corresponds to the true radius and number density of the peak. Thus, it is possible to reconstruct the true position of each initial peak from the discretized distribution. The total number density of particles is then automatically conserved and the transport is analytically computed using Equation (A1). Afterwards, the new distribution is discretized back onto the classes.

For example, starting typically with a distribution composed of several peaks $(r; n^l_{TiN})$, the inclusion densities are grouped into pairs of classes $(r_i; n_i)$ and $(r_{i+1}; n_{i+1})$. The true coordinates of a peak $(r_D; n_D)$ are calculated from the classes densities through:

$$\begin{cases} n_D(t) = n_i + n_{i+1} \\ r_D = \dfrac{n_i \, r_i + n_{i+1} \, r_{i+1}}{n_i + n_{i+1}} \end{cases} \tag{A3}$$

Each peak is then submitted to growth:

$$r_D(t + dt) = r_D(t) + G \cdot dt \tag{A4}$$

The new distribution is then discretized back into classes: the interval in which stands the new radius is searched: $r_D(t + dt) \in [r_{i*}; r_{i*+1}]$. System (A4) is inverted to deduce the new spread (A5) of the peak on the classes:

$$\begin{cases} n_D(t + dt) = n_{i*} + n_{i*+1} \\ r_D(t + dt) = \dfrac{n_{i*} \, r_{i*} + n_{i*+1} \, r_{i*+1}}{n_{i*} + n_{i*+1}} \end{cases} \tag{A5}$$

$$\Longleftrightarrow \begin{cases} n_{i*} = n_D(t + dt) \, \dfrac{r_{i*+1} - r_D(t + dt)}{r_{i*+1} - r_{i*}} \\ n_{i*+1} = n_D(t + dt) - n_{i*} \end{cases} \tag{A6}$$

Equation (A6) is applied two by two for each pair in the particle size distribution, starting from:

- the highest radius if G > 0;
- the lowest radius if G < 0.

Total dissolution of the nitride is supposed to occur if $r_D(t + dt)$ becomes lower than the initial oxide radius.

References

1. Morita, Z.; Kunisada, K. Solubility of nitrogen and equilibrium of Ti-nitride forming reaction in liquid Fe-Ti alloys. *Tetsu-to-Hagané* **1977**, *63*, 1663–1671. doi:10.2355/tetsutohagane1955.63.10_1663. [CrossRef]
2. Kim, W.Y.; Jo, J.O.; Chung, T.I.; Kim, D.S.; Pak, J.J. Thermodynamics of Titanium, Nitrogen and TiN Formation in Liquid Iron. *ISIJ Int.* **2007**, *47*, 1082–1089. doi:10.2355/isijinternational.47.1082. [CrossRef]
3. Yu, K. *Modelinf for Casting and Solidification Processing*; Marcel Dekker Inc.: New York, NY, USA, 2002.
4. Hans, S. Modélisation des Transfers Couples de Chaleur, de Solute et de Quantité de Mouvement lors de la Refusion à l'arc Sous vide (VAR)–Application aux Alliages de Titane. Ph.D. Thesis, Insitut National Polytechnique de Lorraine, Nancy. French, 1995.
5. Evans, D.; Pehlke, R. Equilibria of nitrogen with the refractory metals titanium, zirconium, columbium, vanadium and tantalum in liquid iron. *Trans. Met. Soc. AIME* **1965**, *233*, 1620–1624.
6. Andersso, J.O.; Helander, T.; Hdghmd, L.; Shi, P.; Sundman, B. THERMO-CALC and DICTRA, Computational Tools For Materials Science. *Calphad* **2002**, *26*, 273–312. [CrossRef]
7. Software, T. *Modeling for Casting and Solidification Processing*; Fundation of Computational Thermodynamics: Stockholm, Sweden, 2013.
8. Bertram, L.; Schunk, P.; Kempka, S.; Spadafora, F.; Minisandram, R. The macroscale simulation of remelting processes. *J. Met.* **1998**, *50*, 18–21. [CrossRef]
9. Kelkar, K.; Patankar, S.; Mitchell, A.; Minisandram, R.; Patel, A. Computational Analysis of the Vacuum Arc Remelting (VAR) and Electroslag Remelting (ESR) Processes. *ASM Handbook* **2010**, *22B*, 196–213.
10. Jardy, A.; Ablitzer, D. Solar: numerical software to optimize vacuum arc remelting operations. *Rare. Metal. Mat. Eng.* **2006**, *35*, 119–122.
11. Jardy, A.; Ablitzer, D. Mathematical modelling of superalloy remelting operations. *Mater. Sci. Technol.* **2009**, *25*, 163–169. doi:10.1179/174328408X355406. [CrossRef]
12. Quatravaux, T. Evolution de la Modélisation du Procédé Var—Contribution à la Description de la Dispersion Inclusionnaire dans le puis Liquide et à la Prévention de Défauts de Solidification. Ph.D. Thesis, Insitut National Polytechnique de Lorraine, Nancy, French, 2004.
13. Descotes, V. Précipitation des Inclusions de Nitrure de Titane (TiN) dans un Acier Maraging au Cours de sa Refusion à L'arc électrique Sous Vide. Ph.D. Thesis, Université de Lorraine, Nancy, French, 2014.
14. Patankar, S. *Numerical Heat Reatment and Fluid Flow*; Hemisphere Publishing Crop.: Washington, DC, USA, 1980.
15. Quatravaux, T.; Ryberon, S.; Hans, S.; Jardy, A.; Lusson, B.; Richy, P.; Ablitzer, D. Transient VAR ingot growth modelling: application to specialty steels. *J. Mater. Sci.* **2004**, *39*, 7183–7191. doi:10.1023/B:JMSC.0000048730.26836.68. [CrossRef]
16. Revil-Baudard, M.; Jardy, A.; Combeau, H.; Leclerc, F.; Rebeyrolle, V. Solidification of a Vacuum Arc-Remelted Zirconium Ingot. *Metall. Materi. Trans. B* **2014**, *45*, 51–57. [CrossRef]
17. Jardy, A.; Quatravaux, T.; Ablitzer, D. The Effect of Electromagnetic Stirring on the Turbulent Flow of Liquid Metal in a Vacuum Arc Remelted Ingot. In Proceedings of the 2004 TMS Annual Meeting on Multiphase Phenomena and CFD Modeling and Simulation in Materials Processes, Charlotte, NC, USA, 14–18 March 2004.
18. Lei, H.; Nakajima, K.; He, J. Mathematical Model for Nucleation, Ostwald Ripening and Growth of Inclusion in Molten Steel. *ISIJ Int.* **2010**, *50*, 1735–1745. doi:10.2355/isijinternational.50.1735. [CrossRef]
19. Matsumiya, T. Mathematical Analyses of Segregations and Chemical Compositional Changes of Nonmetallic Inclusions during Solidification of Steels. *Mater. Trans. JIM* **1992**, *33*, 783–794. doi:10.2320/matertrans1989.33.783. [CrossRef]
20. Ohta, H.; Suito, H. Effects of N, C and Si Contents and MgO on Dispersion of TiN Particles in Fe–1.5% Mn–0.05 (0.15)% C Alloy. *Isij Int.* **2007**, *47*, 197–206. doi:10.2355/isijinternational.47.197. [CrossRef]

21. Rocabois, P.; Lehmann, J.; Gaye, H.; Wintz, M. Kinetics of precipitation of non-metallic inclusions during solidification of steel. *J. Cryst. Growth* **1999**, *198-199*, 838–843. doi:10.1016/S0022-0248(98)01139-7. [CrossRef]
22. Lehmann, J.; Rocabois, P.; Gaye, H. Kinetic model of non-metallic inclusions' precipitation during steel solidification. *J. Non-Cryst. Solids* **2001**, *282*, 61–71. doi:10.1016/S0022-3093(01)00329-5. [CrossRef]
23. Descotes, V.; Bellot, J.P.; Witzke, S.; Jardy, A. Modeling the Titanium Nitride (TiN) Germination and Growth during the Solidification of a Maraging Steel. In Proceedings of the 2013 International Symposium on Liquid Metal Processing & Casting, Austin, TX, USA, 22–25 September 2013. doi:10.1007/978-3-319-48102-9_30. [CrossRef]
24. Descotes, V.; Migot, S.; Robaut, F.; Perrin-Guérin, V.; Witzke, S.; Bellot, J.P.; Jardy, A. TEM Characterization of a Titanium Nitride (TiN) Inclusion in a Fe-Ni-Co Maraging Steel. *Metall. Mat. Trans. A* **2015**, *46*, 2793–2795. [CrossRef]
25. Soustelle, M. *Cinétique Hétérogène*; Hermes Science Publications: Paris, French, 2007.
26. Dantzig, J.; Rappaz, M. *Solidification*; EPFL Press: Lausanne, Switzerland, 2009.
27. Kurz, W.; Fischer, D. *Fundamentals of solidification*; Trans Tech Publication LTD: Zurich, Switzerland, 1998.